A Matrix Converter-Based Bidirectional Contactless Grid Interface

Saranga Weerasinghe, *Student Member, IEEE*, Udaya K. Madawala, *Senior Member, IEEE*, and Duleepa J. Thrimawithana, *Member, IEEE*

***Abstract*—Bidirectional contactless grid interfaces based on inductive power transfer technology have shown substantial promise in vehicle-to-grid and grid-to-vehicle applications as an alternative to hardwired interfaces. Such a bidirectional contactless grid interface typically includes a two-stage power conversion in conjunction with a bulky and expensive dc-link capacitor and a large low-frequency inductor to generate voltages at high frequency from low-frequency utility grid. This paper proposes a matrix converter (MC) that directly produces voltages at high frequency from the utility grid to drive resonant networks of the bidirectional contactless interface. A comprehensive mathematical model that predicts the steady-state voltages and currents as well as the power drawn by the system is proposed to gain an insight into the operation of the proposed MC topology. Utilizing the mathematical model, a modulation strategy is also proposed to attenuate the undesirable harmonics in the grid current. Experimental results obtained from a 1-kW prototype system show excellent agreement with those obtained from the mathematical model, validating the practical applicability of the proposed approach. Experimental results of total harmonic distortion of grid currents are also presented to demonstrate the effectiveness of the proposed modulation strategy at attenuation of grid current harmonics.**

***Index Terms*—Grid integration, inductive power transfer (IPT), matrix converter (MC), total harmonic distortion (THD), wireless power transfer.**

I. Introduction

In power transfer technology, inductive power transfer (IPT) has gained the attention of the power electronics community in recent years as a technique for transferring power without any physical contacts. It offers a number of benefits, such as high galvanic isolation, high flexibility, and high reliability particularly in hostile environments. A wide variety of applications of IPT include clean rooms[1], [2], biomedical implants [3]–[5], consumer electronics[6]–[8], and electric vehicle (EV) charging[9]–[13].

With recent advances in battery charging technologies, EVs have been proposed as grid-integrated distributed energy storage devices for storage and retrieval of energy to facilitate dynamic demand management. These, referred to as vehicle-to-grid (V2G) or grid-to-vehicle (G2V) systems, require interfaces that can handle two-way or bidirectional power flow between the grid and EVs [14]–[16]. Although hardwired bidirectional interfaces between the grid and EVs are simple, bidirectional inductive power transfer (BD-IPT) technology has now emerged as an attractive alternative owing to the advantages it offers over hardwired interfaces [12]. However, BD-IPT systems typically operate at much higher frequencies with respect to the grid frequency. As such, grid integration of EVs with BD-IPT generally involves a low-frequency ac-to-dc power conversion as well as a dc-to-high frequency ac power conversion, requiring two or more power electronic converters in conjunction with a large and expensive dc-link capacitor and a bulky low-frequency input inductor [17], [18]. Inclusion of the dc-link capacitor and the input inductor increases the overall cost and size and, thereby, reduces the power density of the system. Moreover, the presence of the dc-link capacitor compromises the overall reliability of the system, since the life time of the dc-link capacitor is affected by external factors such as type of dielectric material used and operating temperatures. Alternatively, a back-to-back converter (BTBC)-based bidirectional grid interface that eliminates a large dc-link capacitor and an input inductor has been proposed in [19] to overcome the drawbacks of conventional grid integrated BD-IPT systems. Even though the BTBC-based system offers numerous benefits in contrast to conventional systems, the grid current of the BTBC-based system becomes discontinuous as the grid voltage approaches zero. This consequently results in a high total harmonic distortion (THD) profile in grid currents that exceeds the limits specified by the IEEE standards 1547 [20]. Hence, a BD-IPT grid interface that is capable of drawing or supplying sinusoidal grid currents without employing bulky and expensive energy storage elements is the preferred solution.

This paper proposes a matrix converter (MC) based grid-integrated BD-IPT interface that ameliorates the aforementioned issues of previously reported bidirectional contactless grid interfaces. Being an ac–ac converter, the MC is capable of deriving a high-frequency ac voltage at its output by converting the input low-frequency grid voltage in the absence of energy storage elements such as inductors or capacitors. The challenge associated with the MC, however, is the commutation of current between switching devices of the MC when feeding inductive loads or current sources as they inherently do not hold any natural freewheeling paths. This is generally achieved by forced commutation of currents based on multistep commutation algorithms [21], [22]. The output of the proposed MC-based BD-IPT system is connected to a tuned inductor–capacitor–capacitor–inductor (LCCL) resonant network that resembles a current

Manuscript received December 18, 2015; revised February 27, 2016; accepted April 7, 2016. Date of publication May 3, 2016; date of current version December 9, 2016. Recommended for publication by Associate Editor S. K. Panda.

The authors are with the Department of Electrical and Computer Engineering, The University of Auckland, Auckland 1010, New Zealand (e-mail: s.weerasinghe@auckland.ac.nz; u.madawala@auckland.ac.nz; d.thrimawithana@auckland.ac.nz).

Color versions of one or more of the figures in this paper are available online at http://ieeexplore.ieee.org.

Digital Object Identifier 10.1109/TPEL.2016.2557963

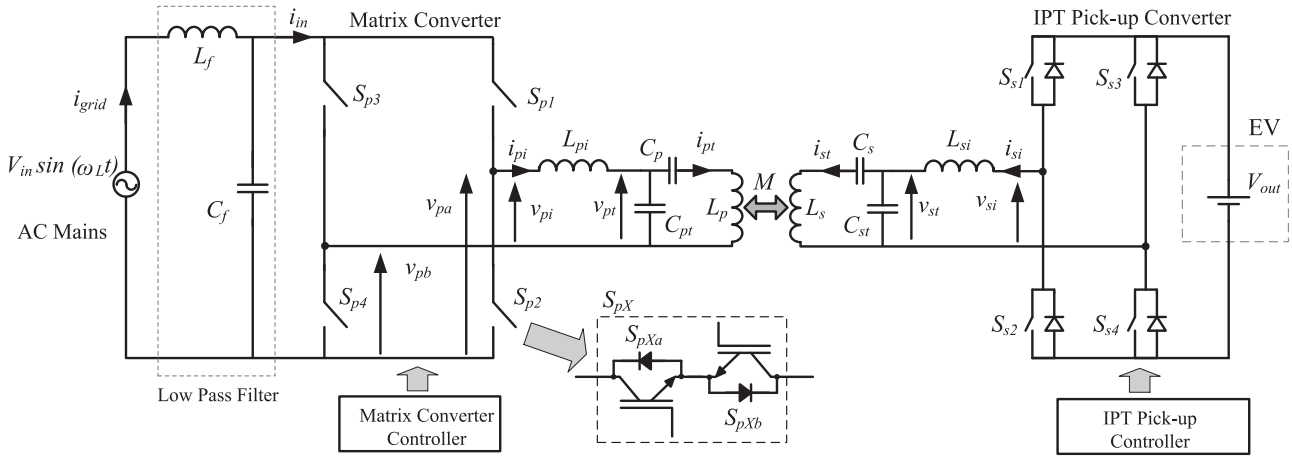

Fig. 1. MC-based grid connected BD-IPT system.

source. As a result, the current commutation of the proposed MC is executed using a commutation algorithm based on its output current direction. To date, an MC topology that is operated using a current commutation algorithm based on the output current direction is yet to be reported for applications similar to BD-IPT systems, where high-order and high-frequency resonant networks are present.

Although several MC topologies have been reported and experimentally validated for series tuned unidirectional IPT systems in [23] and [22], they have been implemented with relative voltage-magnitude-based commutation algorithms. The voltage-magnitude-based commutation algorithms typically require two or more accurate and reliable voltage measurements for a single-phase MC. On the other hand, the current-direction-based commutation algorithms require only one accurate and reliable current measurement for the operation of all four bidirectional switches of a single-phase MC. Even though implementation of current-direction-based commutation algorithms has been challenging in the past as they require relatively fast responsive digital controllers, recent developments in processors and controllers have offered significantly improved processing capabilities. Thus, the adaptation of a current direction based commutation algorithm for the proposed system is more advantageous, since it reduces the component count of the experimental setup.

In order to gain an insight into the steady-state behavior of the proposed system, a comprehensive mathematical model is proposed. Using the mathematical model, a modulation strategy that attenuates grid current harmonics is proposed. The proposed modulation strategy eliminates the need of bulky multistage low-pass filters that are commonly found in MC-based systems [24]. Key parameters such as converter voltages, currents, and grid currents obtained from the proposed mathematical model are compared with those obtained from a 1-kW prototype in order to highlight the practical applicability of the proposed bidirectional contactless grid interface. The effectiveness of the proposed strategy at attenuation of grid current harmonics is also validated using experimental results of THD of grid currents. Experimental results clearly indicate that the proposed MC-based BD-IPT system is able to maintain its grid current harmonics within the limits specified by the IEEE standards 1547 over the majority of its operational range.

II. Proposed MC-Based Inductively Coupled Bidirectional Grid Interface

A. Operation of MC and Commutation Strategy

The proposed MC-based grid connected BD-IPT system is depicted in Fig. 1. As seen from Fig. 1, a single-phase MC and an LCCL network, which is tuned to resonant frequency f_T, constitute the primary side. In contrast to bidirectional inductively coupled grid interfaces reported in [18] and [19], the proposed topology eliminates the input inductor, dc-link capacitor as well as the low-frequency ac–dc–ac two-stage power conversion. Thus, it accomplishes a direct low-frequency ac–high-frequency ac conversion.

As evident from Fig. 1, the MC consists of four bidirectional switches namely, $S_{p1} - S_{p4}$, which should be able to conduct currents and block voltages in both directions. As such, each bidirectional switch is constructed using two back-to-back connected semiconductor switching devices S_{pXa} and S_{pXb}, as shown in Fig. 1, where $X \in \{1, 2, 3, 4\}$.

As presented in Fig. 2(a), during the positive half cycle of the grid voltage $v_{\rm grid}$, the bidirectional switches S_{p1} and S_{p2} are switched at the same resonant frequency f_T with 50% duty cycle by operating their respective switching devices S_{p1a}/S_{p1b} and S_{p2a}/S_{p2b} in order to derive a unipolar positive square wave voltage $v_{\rm pa}$. Similarly, bidirectional switches S_{p3} and S_{p4}, which comprise S_{p3a}/S_{p3b} and S_{p4a}/S_{p4b}, respectively, are also operated at f_T with 50% duty cycle to derive $v_{\rm pb}$. $v_{\rm pb}$ is delayed by φ_1 radians with respect to $v_{\rm pa}$, where $0 \leq \varphi_1 \leq \pi$. The potential difference between $v_{\rm pa}$ and $v_{\rm pb}$ results in a bipolar square wave voltage $v_{\rm pi}$ across the primary LCCL network as shown in Fig. 2(a). The effective value of $v_{\rm pi}$ is proportional to the phase delay φ_1, which is called the primary phase modulation henceforth.

During the negative half cycle of the grid voltage, $S_{p1} - S_{p4}$ are operated in a manner as depicted in Fig. 2(b). As both $v_{\rm pa}$

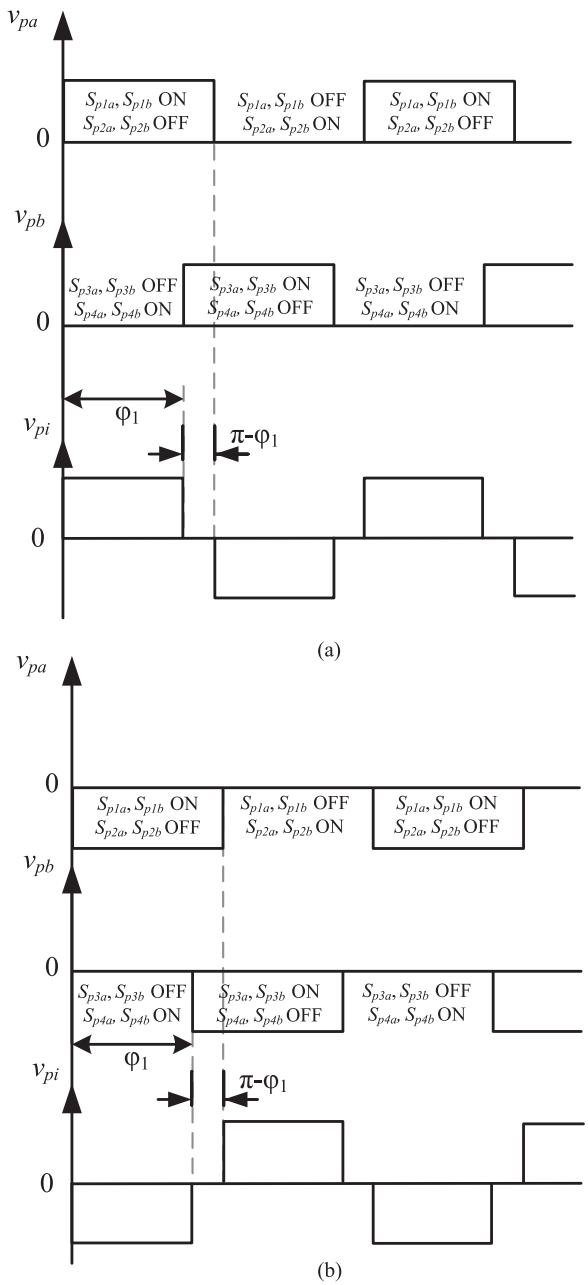

Fig. 2. $V_{\rm pa}$, $V_{\rm pb}$, and $V_{\rm pi}$ over (a) positive half cycle (b) negative half cycle of $v_{\rm grid}$.

and $v_{\rm pb}$ happen to be negative unipolar square wave voltages over the negative half cycle of the grid voltage, $v_{\rm pi}$ is displaced by 180° in contrast to that of the positive half cycle of $v_{\rm grid}$.

It can be shown that the series current $i_{\rm pi}$ of a tuned resonant LCCL network can be generally deduced to a current source [25]. Furthermore, the direction of $i_{\rm pi}$ of a LCCL-tuned BD-IPT system, which consists of a sixth or eighth-order high-frequency resonant network, changes its direction one or more times over a single high-frequency switching cycle. Since the primary phase modulation φ_1, which can take any value between 0 and π radians, determines the switching instances of S_{p3} and S_{p4}, $i_{\rm pi}$ can be either positive or negative at any switching instance. Thus, the current commutation between the bidirectional switches of

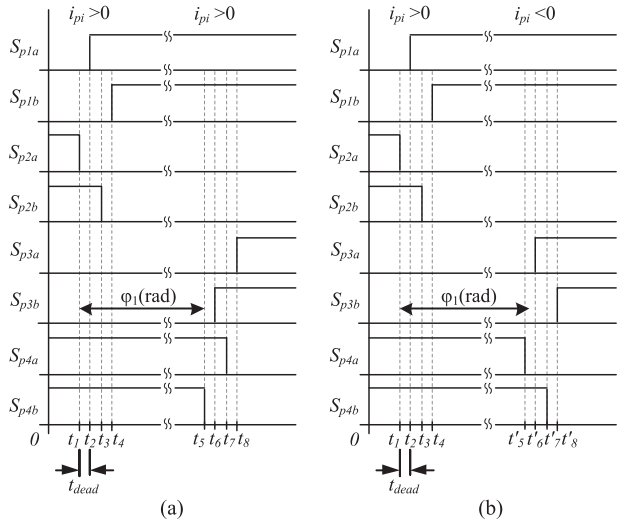

Fig. 3. Gating signals of bidirectional switches for (a) $\varphi_1 = \alpha$ (b) $\varphi_1 = \beta$.

the proposed MC is executed entirely based on the direction of $i_{\rm pi}$ regardless of the grid voltage or the direction of power flow. Therefore, the direction of $i_{\rm pi}$ immediately before the turn ON or turn OFF of each bidirectional switch pair of the two legs is inspected and, accordingly, the turn ON or turn OFF of each bidirectional switch pair is executed in a sequence as explained in Fig. 3(a) and (b).

Fig. 3(a) demonstrates the gating signals for turning OFF S_{p2}, turning ON S_{p1}, turning ON S_{p3} and turning OFF S_{p4} for $\varphi_1 = \alpha$, where $0 < \alpha < \pi$. At $t = t_1$, the bidirectional switch S_{p2} is required to turn OFF, and hence, the direction of $i_{\rm pi}$ is inspected at $t = (t_1 - \delta)$, where $\delta \approx 0$. As $i_{\rm pi}$ occurs to be positive, S_{p2a} is turned OFF at $t = t_1$. Afterwards, the turning ON of S_{p1a}, turning OFF of S_{p2b} and turning ON of S_{p1b} follow a four-step current commutation principle to avoid discontinuities of $i_{\rm pi}$. After a delay of $\varphi_1 = \alpha$ radians, the current direction of $i_{\rm pi}$ is again inspected in order to operate the bidirectional switches S_{p3a}/S_{p3b} and S_{p4a}/S_{p4b}. Owing to the fact that the current direction is positive, S_{p4b} is turned OFF at $t = t_5$, and the switching of S_{p3b}, S_{p4a} and S_{p3a} is executed sequentially at $t = t_6$, $t = t_7$ and $t = t_8$, respectively.

On the other hand, Fig. 3(b) depicts the gating signals of $S_{p1} - S_{p4}$, when the MC is operated at a primary phase modulation φ_1 of β, where $0 < \beta < \pi$ and $\beta \neq \alpha$. In contrast to Fig. 3(a), $i_{\rm pi}$ occurs to be negative after a φ_1 of β radians in Fig. 3(b). Therefore, the turning OFF of S_{p4a}/S_{p4b} and turning ON of S_{p3a}/S_{p3b} follow a different sequence for commutating $i_{\rm pi}$.

As the direction of $i_{\rm pi}$ at switching instances can change with the value of the primary phase modulation φ_1, the current commutation between the bidirectional switches of the proposed MC is executed dynamically by inspecting the direction of $i_{\rm pi}$ immediately before operating any given switching device. Hence, the commutation algorithm of the proposed MC becomes more complex than that of conventional MCs and practically requires a fast responsive controller as well as a current direction detection circuitry with substantially low delays. Nevertheless, $v_{\rm pi}$

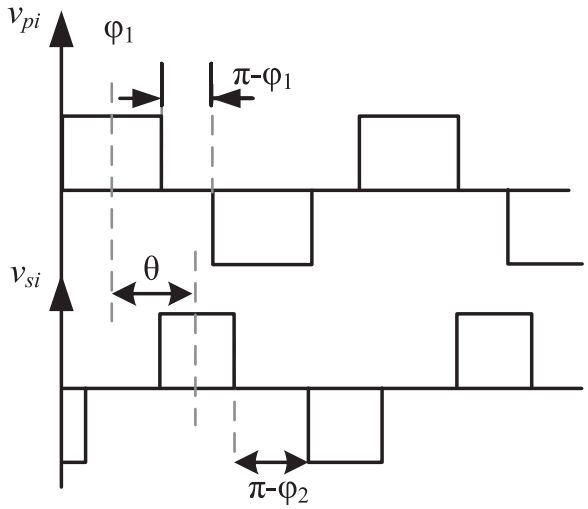

Fig. 4. Pick-up converter output voltage $v_{\rm si}$ over the positive half cycle of $v_{\rm grid}$.

manifests $i_{\rm pt}$ in the primary winding L_p, which is magnetically coupled to the pick-up winding L_s.

B. Operation of IPT Pick-Up Converter

The pick-up side of the proposed system, shown in Fig. 1, consists of another LCCL network tuned to the same resonant frequency, a full-bridge converter known as the IPT primary converter, and a dc voltage source $V_{\rm out}$ to represent an EV for simplicity. Depending on the direction of the power flow, the pick-up has the ability to function as either a source or an active load. The operation of the IPT pick-up converter is defined based on the phase modulation principle similar to that of MC. Hence, $S_{s1} - S_{s4}$ of the IPT pick-up converter are operated at f_T with 50% duty cycle with a pick-up phase modulation φ_2 in order to produce $V_{\rm si}$, as shown in Fig. 4, regardless of the direction of power flow. In addition, a relative phase angle of θ is maintained between $v_{\rm pi}$ and $v_{\rm si}$, where $-\pi/2 \leq \theta \leq \pi/2$. Furthermore, φ_2 can vary between 0 and π radians over the positive half cycle of $v_{\rm grid}$. Over the negative half cycle of $v_{\rm grid}$, $v_{\rm pi}$ becomes inverted as previously explained and as a result, φ_2 is varied between 0 and $-\pi$ over the negative half cycle of $v_{\rm grid}$. Therefore, the relative phase angle θ between $v_{\rm pi}$ and $v_{\rm si}$ remains fixed over both the positive and the negative half cycles. In order to maintain the power factor of BD-IPT system at unity, θ is fixed at $\pm\frac{\pi}{2}$ radians [12].

III. Steady-State Mathematical Model

A. Currents and Voltages of the Resonant Network

In order to gain an insight into the operation of the proposed MC-based BD-IPT interface, the following steady-state mathematical model is proposed.

The grid voltage $v_{\rm grid}$ is assumed to be a sinusoidal voltage source at an angular frequency of ω_L. Hence, $v_{\rm grid}$ can be expressed in the time domain as

$$v_{\rm grid} = V_{\rm in}\ \sin(\omega_L t) \tag{1}$$

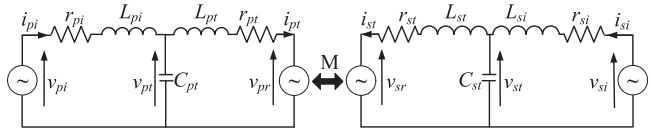

Fig. 5. LCL network of the proposed scheme.

where $V_{\rm in}$ is the peak grid voltage.

The periodic time of a switching cycle of the MC is much larger than dead time $t_{\rm dead}$ between each switching device of the MC as shown in Fig. 3(a) and (b). Therefore, the effect of $t_{\rm dead}$ on $v_{\rm pi}$ is assumed to be negligible. As such, $v_{\rm pi}$ can be derived as

$$v_{\rm pi}(t) = V_{\rm in}\ \sin(\omega_L t)\,\frac{4}{\pi}\sum_{n=1,3..}^{\infty}\frac{1}{n}\cos\left(n\omega_T t\right)\,\sin\left(\frac{n\varphi_1}{2}\right). \tag{2}$$

Further simplification of (2) results in

$$v_{\rm pi}(t) = \frac{2V_{\rm in}}{\pi}\sum_{n=1,3..}^{\infty}\frac{1}{n}\sin\left(\frac{n\varphi_1}{2}\right)\begin{bmatrix}\sin\left(n\omega_T+\omega_L\right)t\\ -\sin\left(n\omega_T-\omega_L\right)t\end{bmatrix}. \tag{3}$$

Similarly, the pick-up converter output voltage $v_{\rm si}$ in the time domain can be written as

$$v_{\rm si}(t) = V_{\rm out}\,\frac{4}{\pi}\sum_{n=1,3..}^{\infty}\frac{1}{n}\cos\left(n\omega_T t + n\theta\right)\,\sin\left(\frac{n\varphi_2}{2}\right). \tag{4}$$

The LCCL network, shown in Fig. 1, can be further simplified by defining equivalent impedances $Z_{\rm pt}$ for L_p,C_p on the primary side and $Z_{\rm st}$ for L_s,C_s on the pick-up side, respectively. As such, $Z_{\rm pt} = L_p\omega - 1/\omega C_p$ and $Z_{\rm st} = L_s\omega - 1/\omega C_s$, for any angular frequency ω. Both $Z_{\rm pt}$ and $Z_{\rm st}$ behave inductively over the range of frequencies considered in this paper. Therefore, they can be replaced by equivalent inductances $L_{\rm pt}$ and $L_{\rm st}$ as, $L_{\rm pt} = L_p - \frac{1}{\omega^2 C_p}$ and $L_{\rm st} = L_s - \frac{1}{\omega^2 C_s}$, respectively. As a result, the LCCL network can be simplified to an inductor–capacitor–inductor (LCL) network with their respective equivalent series resistances (ESRs) as illustrated in Fig. 5. Due to mutual coupling M, the induced voltages $V_{\rm pr}$ and $V_{\rm sr}$ from $I_{\rm st}$ and $I_{\rm pt}$ can be written as $V_{\rm pr} = j\omega\, M I_{\rm st}$ and $V_{\rm sr} = j\omega\, M I_{\rm pt}$, respectively, where $M = k\sqrt{L_p L_s}$ and k is the coefficient of coupling.

It is learnt from (3) that $v_{\rm pi}$ can be transformed into two phasors $V_{\rm piA}$ and $V_{\rm piB}$ with a magnitude of $\frac{2V_{\rm in}}{\pi}\frac{1}{n}\sin(\frac{n\varphi_1}{2})$ rotating at $(nw_T + w_L)$ and $(nw_T - w_L)$, respectively, where $n \in \{1, 3, 5, \ldots\}$. Similarly, $v_{\rm si}$ can be transformed into another phasor $V_{\rm out}\,\frac{4}{n\pi}\,\sin(\frac{n\varphi_2}{2})\,(\cos\, n\theta + j\sin\, n\theta)$ rotating at nw_T. Using the superposition theorem, the LCL networks, shown in Fig. 5, can be analyzed in the phasor domain under three distinct frequencies given by $\omega_A = nw_T + w_L$,$\omega_B = nw_T - w_L$ and $\omega_C = nw_T$.

Case A: $V_{\rm piA} = \frac{2V_{\rm in}}{n\pi}\sin(\frac{n\varphi_1}{2})$ rotating at an angular speed of ω_A and $V_{\rm siA} = 0$.

Using the analysis presented in [25] for an LCL network

$$I_{\mathrm{piA}} = \frac{1}{Z_{\mathrm{prA}} + j\omega_A L_{\mathrm{piA}} + r_{\mathrm{pi}}} \left[-I_{\mathrm{prA}} Z_{\mathrm{prA}} + V_{\mathrm{piA}}\right] \quad (5)$$

$$I_{\mathrm{siA}} = \frac{1}{Z_{\mathrm{srA}} + j\omega_A L_{\mathrm{siA}} + r_{\mathrm{si}}} \left[-I_{\mathrm{srA}} Z_{\mathrm{srA}}\right] \quad (6)$$

$$I_{\mathrm{ptA}} = \frac{1}{K_A} \left[I_{\mathrm{inA}} \frac{Z_{\mathrm{pa}}}{Z_{\mathrm{pa}} + j\omega_A L_{\mathrm{ptA}} + r_{\mathrm{pt}}} \right] \quad (7)$$

$$I_{\mathrm{stA}} = \frac{1}{K_A} \left[I_{\mathrm{inA}} \frac{\frac{j\omega_A M Z_{\mathrm{pa}}}{(Z_{\mathrm{pa}} + j\omega_A L_{\mathrm{ptA}} + r_{\mathrm{pt}})}}{\cdot \frac{1}{(Z_{\mathrm{sA}} + j\omega_A L_{\mathrm{stA}} + r_{\mathrm{st}})}} \right] \quad (8)$$

where

$$I_{\mathrm{inA}} = \frac{V_{\mathrm{piA}}}{r_{\mathrm{pi}} + j\omega_A L_{\mathrm{pi}}}, I_{\mathrm{prA}} = \frac{j\omega_A M}{j\omega_A L_{\mathrm{pt}} + r_{\mathrm{pt}}} I_{\mathrm{stA}},$$

$$I_{\mathrm{srA}} = \frac{j\omega_A M}{j\omega_A L_{\mathrm{st}} + r_{\mathrm{st}}} I_{\mathrm{ptA}}, Z_{\mathrm{pa}} = \frac{j\omega_A L_{\mathrm{pi}} + r_{\mathrm{pi}}}{1 - \omega_A^2 L_{\mathrm{pi}} C_{\mathrm{pt}} + j\omega_A C_{\mathrm{pt}} r_{\mathrm{pi}}},$$

$$Z_{\mathrm{sA}} = \frac{j\omega_A L_{\mathrm{si}} + r_{\mathrm{si}}}{1 - \omega_A^2 L_{\mathrm{si}} C_{\mathrm{st}} + j\omega_A C_{\mathrm{st}} r_{\mathrm{si}}},$$

$$Z_{\mathrm{prA}} = \frac{j\omega_A L_{\mathrm{ptA}} + r_{\mathrm{pt}}}{1 - \omega_A^2 L_{\mathrm{ptA}} C_{\mathrm{pt}} + j\omega_A C_{\mathrm{pt}} r_{\mathrm{pt}}},$$

$$\mathrm{Z_{srA}} = \frac{\mathrm{j\omega_A\ L_{stA} + r_{st}}}{1 - \omega_A{}^2 \mathrm{L_{stA}\, C_{st}} + \mathrm{j\omega_A}\, C_{\mathrm{st}} r_{\mathrm{st}}}$$

and

$$K_A = 1 + \frac{\omega_A^2 M^2}{(Z_{\mathrm{pa}} + j\omega_A L_{\mathrm{ptA}} + r_{\mathrm{pt}})(Z_{\mathrm{sA}} + j\omega_A L_{\mathrm{stA}} + r_{\mathrm{st}})}.$$

Similarly, expressions for I_{ptB}, I_{stB}, I_{piB}, and I_{siB} can also be derived for Case B, where $V_{\mathrm{piB}} = \frac{-2V_{\mathrm{in}}}{n\pi} \sin(\frac{n\varphi_1}{2})$ rotating at an angular speed of ω_B and $V_{\mathrm{siB}} = 0$.

Case C: $V_{\mathrm{piC}} = 0$ and $V_{\mathrm{siC}} = V_{\mathrm{out}} \frac{4}{n\pi} \sin(\frac{n\varphi_2}{2})[\cos(n\theta) + j \sin(n\theta)]$ rotating at an angular speed of ω_C.

As V_{piC} is short circuited, I_{piC}, I_{siC}, I_{ptC}, and I_{stC} can be given by

$$I_{\mathrm{piC}} = \frac{1}{Z_{\mathrm{prC}} + j\omega_C L_{\mathrm{piC}} + r_{\mathrm{pi}}} \left[-I_{\mathrm{prC}} Z_{\mathrm{prC}}\right] \quad (9)$$

$$I_{\mathrm{siC}} = \frac{1}{Z_{\mathrm{srC}} + j\omega_C L_{\mathrm{siC}} + r_{\mathrm{si}}} \left[-I_{\mathrm{srC}} Z_{\mathrm{srC}} + V_{\mathrm{siC}}\right] \quad (10)$$

$$I_{\mathrm{ptC}} = \frac{1}{K_C} \left[\frac{I_{\mathrm{outC}} \frac{j\omega_C M Z_{\mathrm{sC}}}{(Z_{pC} + j\omega_C L_{\mathrm{ptC}} + r_{\mathrm{pt}})}}{\cdot \frac{1}{(Z_{\mathrm{sC}} + j\omega_C L_{\mathrm{stC}} + r_{\mathrm{st}})}} \right] \quad (11)$$

$$I_{\mathrm{stC}} = \frac{1}{K_C} \left[I_{\mathrm{outC}} \frac{Z_{\mathrm{sC}}}{Z_{\mathrm{sC}} + j\omega_C L_{\mathrm{stC}} + r_{\mathrm{st}}} \right] \quad (12)$$

where $I_{\mathrm{outC}} = \frac{V_{\mathrm{siC}}}{r_{\mathrm{si}} + j\omega_C L_{\mathrm{si}}}$, I_{prC}, I_{srC}, Z_{pC}, Z_{sC}, Z_{prC}, Z_{srC}, and K_C can be obtained for ω_C by using the respective equations given in Case A for ω_A.

Using I_{piA}, I_{piB}, and I_{piC} in the phasor domain, i_{pi} in the time domain can be derived as

$$i_{\mathrm{pi}}(t) = \sum_{n_1=1,3..}^{\infty} |I_{\mathrm{piA}}| \sin\left[(n_1\omega_T + \omega_L)\, t + \arg\left(I_{\mathrm{piA}}\right)\right] + \sum_{n_2=1,3..}^{\infty} |I_{\mathrm{piB}}| \sin\left[(n_2\omega_T - \omega_L)\, t + \arg\left(I_{\mathrm{piB}}\right)\right] + \sum_{n_3=1,3..}^{\infty} |I_{\mathrm{piC}}| \cos\left[n_3\omega_T t + \arg\left(I_{\mathrm{piC}}\right)\right]. \quad (13)$$

Although, $i_{\mathrm{si}}(t)$, $i_{\mathrm{pt}}(t)$, and $i_{\mathrm{st}}(t)$ can also be calculated in a similar manner, they are not shown here due to space limitations.

B. Grid Currents

The input current $i_{\mathrm{in}}(t)$ of the MC can be given based on the operation of the bidirectional switches $S_{p1} - S_{p4}$ of the MC as

$$i_{\mathrm{in}}(t) = \begin{cases} i_{\mathrm{pi}}(t), & \text{if } S_{p1} \;\&\; S_{p4} \text{ ON} \\ -i_{\mathrm{pi}}(t), & \text{if } S_{p2} \;\&\; S_{p3} \text{ ON} \\ 0, & \text{otherwise.} \end{cases}$$

As such, $i_{\mathrm{in}}(t)$ can be obtained by multiplication of $i_{\mathrm{pi}}(t)$ with a function $f_{\mathrm{mc}}(t)$ that models the operation of bidirectional switches $S_{p1} - S_{p4}$ in the time domain as

$$i_{\mathrm{in}}(t) = i_{\mathrm{pi}}(t) \cdot f_{\mathrm{mc}}(t) \quad (14)$$

where $f_{\mathrm{mc}}(t) = \frac{4}{\pi} \sum_{n=1,3..}^{\infty} \frac{1}{n} \cos(n\omega_T t) \sin\left(\frac{n\varphi_1}{2}\right)$.

Although the grid current $i_{\mathrm{grid}}(t)$ of the system can be derived using (14), it is a tedious procedure due to the complexity of $i_{\mathrm{pi}}(t)$ given by (13).

However, as both the primary and the pick-up LCL networks are turned to the resonant frequency

$$\omega_T{}^2 = \frac{1}{L_{\mathrm{pi}} C_{\mathrm{pt}}} = \frac{1}{L_{\mathrm{pt}} C_{\mathrm{pt}}} = \frac{1}{L_{\mathrm{si}} C_{\mathrm{st}}} = \frac{1}{L_{\mathrm{st}} C_{\mathrm{st}}}.$$

Furthermore, $\omega_T \ggg \omega_L$ and ESRs of inductors are negligibly small. Therefore, $I_{\mathrm{piA}} \approx 0$, $I_{\mathrm{piB}} \approx 0$ and $I_{\mathrm{piC}} = \frac{j\, M\, V_{\mathrm{si}}}{\omega_C\, L_{\mathrm{pt}}\, L_{\mathrm{si}}}$.

Hence, in the time domain $i_{\mathrm{pi}}(t)$ can be simplified to

$$i_{\mathrm{pi}}(t) = \sum_{n=1,3..}^{\infty} \frac{4MV_{\mathrm{out}} \sin\left(\frac{n\varphi_2}{2}\right)}{n^2 \pi \omega_T L_{\mathrm{pt}} L_{\mathrm{si}}} \cos\left[n\omega_T t + \frac{\pi}{2} + n\theta\right]. \quad (15)$$

In the presence of the inductor–capacitor (LC) low-pass filter, higher order harmonics of the grid current are alleviated. From (14) and (15), i_{grid} can be evaluated by considering only the fundamental frequency components of $i_{\mathrm{pi}}(t)$ and $f_{\mathrm{mc}}(t)$ as

$$i_{\mathrm{grid}}(t) = \frac{V_{\mathrm{in}} L_f C_f \sin\left(\omega_L t + \frac{\pi}{2}\right)}{1 - \omega_L^2 L_f C_f} - \frac{\psi \sin(2\omega_T t + \theta)}{1 - 4\omega_T^2 L_f C_f} - \psi \sin\theta \quad (16)$$

where $\psi = \frac{8}{\pi^2} \frac{M}{\omega_T L_{\mathrm{pt}} L_{\mathrm{si}}} V_{\mathrm{out}} \sin\left(\frac{\varphi_1}{2}\right) \sin\left(\frac{\varphi_2}{2}\right)$.

By analyzing (1), it can be learnt that i_{grid} consists of a low-frequency reactive current component $\frac{V_{\mathrm{in}} L_f C_f \sin\left(\omega_L t + \frac{\pi}{2}\right)}{1 - \omega_L^2 L_f C_f}$, high-frequency current component $\frac{\psi \sin(2\omega_T t + \theta)}{1 - 4\omega_T^2 L_f C_f}$, and low-frequency active current component $\psi \sin\theta$, which is the most dominant term denoted by $i_{\mathrm{grid,dom}}$. Hence

$$i_{\mathrm{grid,dom}}(t) = \frac{8}{\pi^2} \frac{M}{\omega_T L_{\mathrm{pt}} L_{\mathrm{si}}} V_{\mathrm{out}} \sin\left(\frac{\varphi_1}{2}\right) \sin\left(\frac{\varphi_2}{2}\right) \sin\theta. \quad (17)$$

From (17), it can be observed that $i_{\mathrm{grid,dom}}$ is independent of v_{grid}. Hence, $i_{\mathrm{grid,dom}}$ can be considered as a current source.

C. Attenuation of Grid Current Harmonics

It is evident from (17) that $i_{\mathrm{grid,dom}}$ is a square wave at ω_L for fixed φ_1 and φ_2, since all the other parameters of (17) are fixed. Hence, $i_{\mathrm{grid,dom}}$ and, subsequently, i_{grid} contains significantly low-order harmonics. Therefore, attenuation of grid current harmonics of the proposed system is achieved by the modulation of φ_2, utilizing the current source nature of the grid currents as described below.

Suppose $i_{\mathrm{grid,dom}}$ is purely sinusoidal and in-phase with v_{grid} for a given operating mode

$$i_{\mathrm{grid,dom}}(t) = \hat{i}_{\mathrm{grid,dom}} \sin(\omega_L t). \tag{18}$$

From (17), (18) and assuming φ_1 and θ are constants

$$\sin\left(\frac{\varphi_2}{2}\right) = \sin(\omega_L t). \tag{19}$$

Thus, φ_2 can be simplified as

$$\varphi_2 = \frac{4\pi}{T_L} t \tag{20}$$

where T_L is the periodic time of v_{grid}.

Therefore, φ_2 is linearly modulated according to (20) in order to attenuate harmonics and produce near-sinusoidal grid currents, which are in-phase with the grid voltage.

D. Active Power Drawn From the Grid

Out of the grid current components, it is found out that only $i_{\mathrm{grid,dom}}$ contributes to active power delivery. Hence, the active power drawn from the grid over one grid cycle can be defined as

$$P_{\mathrm{in}} = \frac{1}{T_L} \int_0^{T_L} v_{\mathrm{grid}}(t) \left[-i_{\mathrm{grid,dom}}(t)\right] dt. \tag{21}$$

Substitution of (1), (17), and (19) in (21) results in

$$P_{\mathrm{in}} = \frac{-4MV_{\mathrm{in}}V_{\mathrm{out}}}{\pi^2 \omega_T L_{\mathrm{pt}} L_{\mathrm{si}}} \sin\left(\frac{\varphi_1}{2}\right) \sin\theta. \tag{22}$$

As seen from (22), the MC-based BD-IPT system draws power from the grid for $\theta < 0$, while it delivers power into the grid for $\theta > 0$. Additionally, the magnitude of power can be regulated using φ_1.

IV. Experimental Results

A. Hardware Setup

In order to validate the proposed MC topology and modulation strategy experimental results obtained from a 1-kW prototype system, shown in Fig. 6, are presented in this section. Both the MC and the IPT pick-up converter were constructed using Infineon IKW20N60H3 IGBTs. The operating frequency of the prototype system must be selected based on various considerations such as switching losses, size of inductors and pads, and permitted current sensor delays. Although a higher switching frequency reduces the size and cost of the inductors and pads, it increases the switching losses of the converters. Furthermore, the delays in the current sensors and the controllers have to be further reduced to safe current commutation of the MC at a higher operating frequency. Therefore, an operating frequency of 20 kHz was selected to make a compromise between the aforementioned considerations. However, for an EV charging system with a higher power rating, a much higher operating frequency can be more advantageous as the increase in switching loss and reduction of permitted current sensor delays can be outweighed by the significant reduction in the size and cost of inductors as well as pads. A small low-pass LC filter, which comprises an inductor of 80 μH as well as a capacitor of 4.7 μF was employed between the 230 V/50 Hz ac grid and the MC. The IPT pick-up converter was fed by a 220 V dc voltage source with an active load connected in parallel. Double-D-type IPT pads were employed as both primary and pick-up windings at an air gap of 170 mm. Additional parameters of the prototype are provided in Table I.

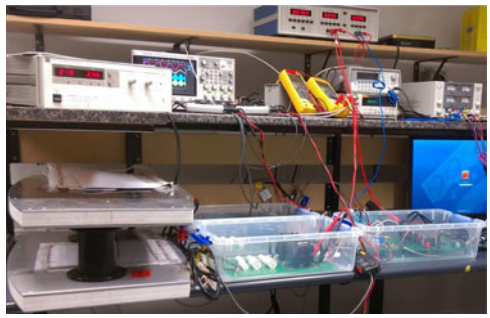

Fig. 6. 1-kW prototype of the MC-based BD-IPT system.

TABLE I
Parameters of the Prototype

Parameter	Value
V_{in}	325 V
V_{out}	220 V
L_{pi} and L_{si}	100 μH
L_p and L_s	147 μH
C_{pt} and C_{st}	0.66 μF
C_p and C_s	1.16 μF
r_{pi} and r_{si}	16 mΩ
r_{pt} and r_{st}	39 mΩ
L_f	80 μH
C_f	4.7 μF
k	0.29
f_T	20 kHz
$P_{\mathrm{in,max}}$	1 kW

As illustrated in Fig. 7, the output current of the MC was sensed and passed through a zero-crossing detector circuit, which consisted of an amplifier and a fast responsive comparator, to determine the direction of the current. Based on the direction of the output current, gating signals for the MC with appropriate dead times were generated by an Altera Cyclone II field programmable gate array. The IPT pick-up converter

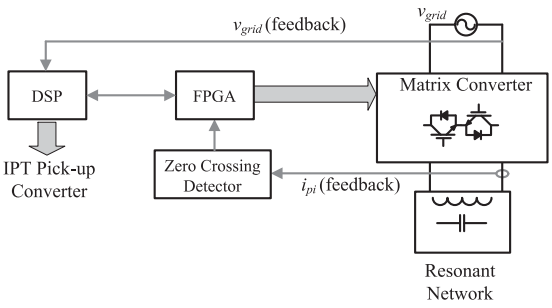

Fig. 7. Block diagram of hardware setup.

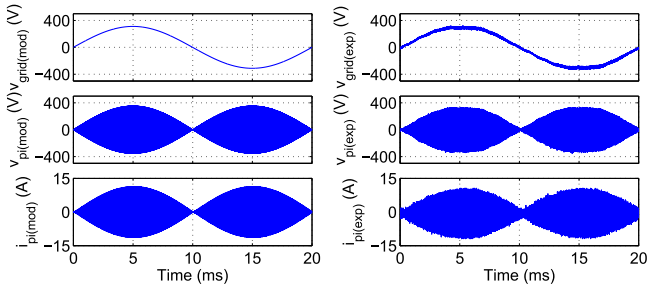

Fig. 8. $v_{\rm grid}$, $v_{\rm pi}$, and $i_{\rm pi}$ for maximum power flow at $\varphi_1 = \pi$ and $\theta = -\pi/2$. (a) Theoretical and (b) experimental.

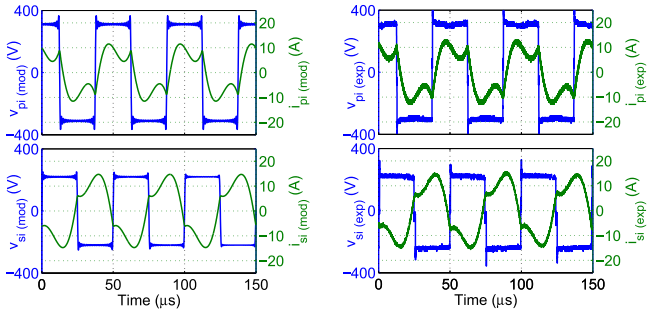

Fig. 9. $v_{\rm pi}$, $i_{\rm pi}$, $v_{\rm si}$, and $i_{\rm si}$ for maximum power in forward direction at $\varphi_1 = \pi$ and $\theta = -\pi/2$. (a) Theoretical and (b) experimental.

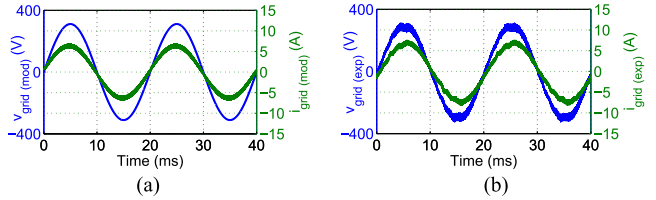

Fig. 10. $i_{\rm grid}$ for maximum power in forward direction at $\varphi_1 = \pi$ and $\theta = -\pi/2$. (a) Theoretical and (b) experimental.

was driven by gating signals produced by a Texas Instruments TMS320F28335 digital signal processor (DSP). A phase-locked loop (PLL) was realized on the DSP in order to detect the phase as well as the frequency of the grid voltage and linearly modulate φ_2 for attenuating grid current harmonics.

B. Steady-State Waveforms

Steady-state waveforms of the MC output voltage $v_{\rm pi}$ and current $i_{\rm pi}$, obtained from both the mathematical model and the prototype over a single cycle of the grid voltage when the power flows from the primary to the pickup at $\varphi_1 = \pi$ and $\theta = -\pi/2$, are depicted in Fig. 8(a) and (b), respectively. Due to the presence of low-order harmonics, the shape of $V_{\rm grid}$, shown in Fig. 8(b), is slightly distorted from a pure sinusoidal. As evident from Fig. 8(a) and (b), both $v_{\rm pi}$ and $i_{\rm pi}$ follow a low-frequency envelope at twice the grid frequency. The presence of $V_{\rm in}\ \sin(\omega_L t)$ term in (2) produces an envelope in $v_{\rm pi}$, whereas the low-frequency envelope in $i_{\rm pi}$ is produced by the linear modulation of φ_2 according to (20). The gains of the PLL used for detecting the phase of $v_{\rm grid}$ are not optimized and hence, a delay of approximately 5° has resulted in the low-frequency envelope of $i_{\rm pi}$ with respect to $v_{\rm grid}$ in Fig. 8(b). Nevertheless, the experimental results obtained from the prototype show good agreement with those obtained from the mathematical model validating its accuracy.

Fig. 9(a) and (b) shows theoretical and experimental results over three cycles at fundamental frequency, respectively, for $v_{\rm pi}$, $i_{\rm pi}$, $v_{\rm si}$, and $i_{\rm si}$ when the system is operated with the same parameters as in the previous case. Although $v_{\rm pi}$ and $i_{\rm pi}$ follow envelopes at 100 Hz as displayed in Fig. 8, the results of $v_{\rm pi}$ and $i_{\rm pi}$ depicted in Fig. 9(a) and (b) were acquired when $v_{\rm grid} \approx V_{\rm in}$ at $t \approx T_L/4$. Since $\omega_T \ggg \omega_L$, both $v_{\rm pi}$ and $i_{\rm pi}$ display constant magnitudes over the considered time frame of 150 μs as shown in Fig. 9(a) and (b). Furthermore, the pick-up phase modulation φ_2 reaches π radians according to (20) at $t = T_L/4$. Hence, $v_{\rm si}$ takes a form of a bipolar square wave with 100% duty cycle. The system is expected to deliver its maximum power in the forward direction, i.e., from the grid to the EV as $v_{\rm si}$ lags $v_{\rm pi}$ with θ set to $-\pi/2$. Both the theoretical and experimental results show that $v_{\rm pi}$ and $i_{\rm pi}$ are reasonably in-phase with each other, making the reactive power requirement minimum. The theoretical results shown in Fig. 9(a) show excellent agreement with the experimental results shown in Fig. 9(b). Thus, the accuracy of the proposed mathematical model for $v_{\rm pi}$, $i_{\rm pi}$, $v_{\rm si}$, and $i_{\rm si}$ is validated for forward and maximum power flow.

Theoretical and experimental results of $i_{\rm grid}$ over a time frame of 40 ms are illustrated in Fig. 10(a) and (b), respectively, for the same operational parameters. From Fig. 9(b), it can be seen that $i_{\rm grid}$ obtained experimentally is necessarily in-phase with $v_{\rm grid}$ primarily due to the low reactive power requirement of the system. As a result, a high power factor of 0.93 was measured. The slight deviation of the power factor from unity can be attributed to the LC low-pass filter, tuning imperfections, and phase errors of PLL. Although the system is supposed to draw about 980 W from the grid according to (22), practically it draws about 1080 W from the grid due to the presence of losses. In general, both theoretical and experimental results of $i_{\rm grid}$ are in good agreement. Thus, the accuracy of the proposed model for $i_{\rm grid}$ as well as the system' s capability to supply maximum power in the forward direction is validated.

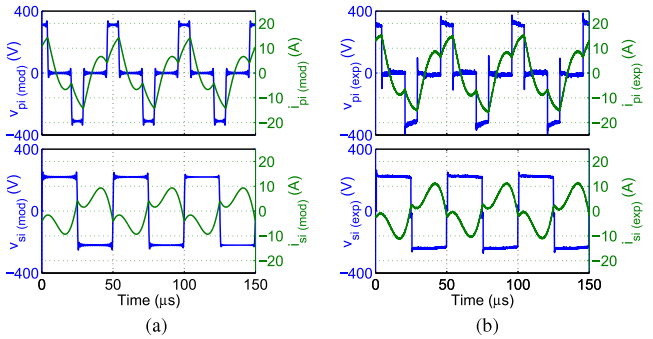

Fig. 11. $v_{\rm pi}$, $i_{\rm pi}$, $v_{\rm si}$, and $i_{\rm si}$ for half power in forward direction at $\varphi_1 = \pi/3$ and $\theta = -\pi/2$. (a) Theoretical and (b) experimental.

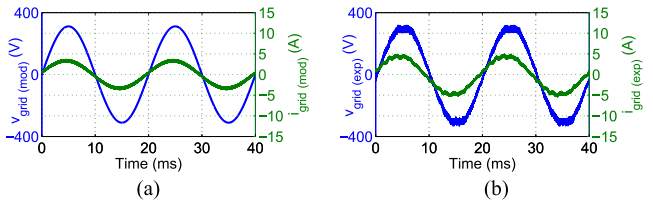

Fig. 12. $i_{\rm grid}$ for half power in forward direction at $\varphi_1 = \pi/3$ and $\theta = -\pi/2$. (a) Theoretical and (b) experimental.

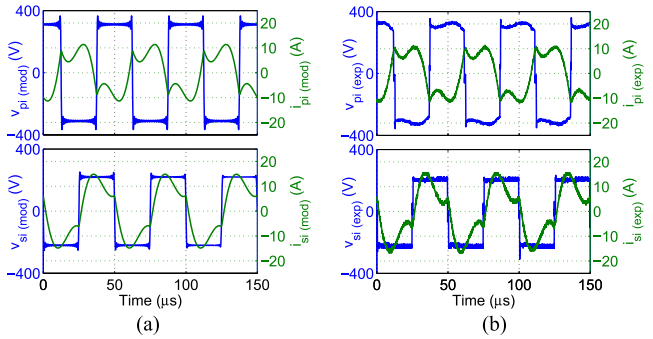

Fig. 13. $v_{\rm pi}$, $i_{\rm pi}$, $v_{\rm si}$, and $i_{\rm si}$ for maximum power in reverse direction at $\varphi_1 = \pi$ and $\theta = \pi/2$. (a) Theoretical and (b) experimental.

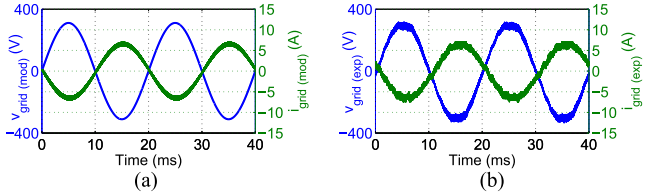

Fig. 14. $i_{\rm grid}$ for maximum power in reverse direction at $\varphi_1 = \pi$ and $\theta = \pi/2$. (a) Theoretical and (b) experimental.

The prototype was operated with a reduced φ_1 of $\pi/3$ radians and θ of $-\pi/2$ radians to demonstrate its ability to regulate the magnitude of the power flow. Theoretical and experimental results of $v_{\rm pi}$, $i_{\rm pi}$, $v_{\rm si}$, and $i_{\rm si}$ were captured at $v_{\rm grid} = V_{\rm in}$ and presented in Fig. 11(a) and (b), respectively. As predicted from (6), the decrease in the duty cycle of $v_{\rm pi}$ has resulted in a decrease in the magnitude of $i_{\rm si}$ in contrast to that of Fig. 9. Furthermore, the direction of $i_{\rm pi}$ changes twice over one fundamental. Therefore, the time difference between the change of current direction and the subsequent switching instance of the corresponding bidirectional switch for current commutation is much lower in this situation. Fig. 12(a) and (b) portrays theoretical and experimental results of $i_{\rm grid}$, respectively. Although the system is supposed to be drawing 490 W, which is half the power drawn at $\varphi_1 = \pi$, the prototype draws approximately 570 W due to losses. Overall, both the theoretical and experimental results are consistent with each other, and thereby validate the mathematical model.

As discussed in Section III-D, negative values of θ contribute to forward power flow, whereas positive values of θ contribute to reverse power flow. Therefore, the prototype was operated with a θ of $\pi/2$ and φ_1 of π for the maximum power flow in the reverse direction. Experimental results as well as the results obtained from the mathematical model are shown in Figs. 13 and 14. In contrast to Fig. 9(a) and (b), $v_{\rm si}$ of Fig. 13(a) and (b) leads $v_{\rm pi}$ by $\pi/2$ radians. Furthermore, the directions of $i_{\rm pi}$ and $i_{\rm si}$ are reversed in Fig. 13(a) and (b) indicating the reversal of power flow. Similarly, the direction of $i_{\rm grid}$ in Fig. 14(a) and (b) is also reversed, even though the magnitude of $i_{\rm grid}$ is roughly equal to that shown in Fig. 10(a) and (b) for the forward power operation. As predicted by (22), the power supplied to grid by the prototype is about 970 W with a power factor of 0.92. Since the results obtained from the mathematical model are sufficiently agreeing with those obtained from the prototype, the accuracy of the mathematical model is proven for the reverse power flow too.

C. Grid Current Harmonics

In order to observe the effectiveness of the modulation strategy presented in Section III-C for attenuation of grid harmonics, experimental results of magnitudes of harmonics of $i_{\rm grid}$ are shown in Fig. 15. Odd and even magnitudes up to the ninth harmonic are shown in Fig. 15(a) and (b) for forward and reverse power flow, respectively, at $\pi/3 \leq \varphi_1 \leq \pi$, which correspond to a power rating from 0.5 to 1 p.u. As explained in Section III-C, $i_{\rm grid}$ is expected to take a form of a bipolar square wave at ω_L with significant amount of low-order odd harmonics if any modulation strategy was not employed. The impact of the modulation strategy on $i_{\rm grid}$ is clearly visible in Fig. 15(a) and (b), as each odd harmonic of $i_{\rm grid}$ is reduced to a maximum of approximately 2% in either direction of power flow. Even though the modulation strategy is supposed to produce a pure sinusoidal $i_{\rm grid,dom}$ waveform that only contributes to active power flow under ideal conditions, the prototype is expected to draw small reactive current components due to the slight detuning of the primary LCCL network. As such, presence of low-order harmonics in $i_{\rm grid}$, though their magnitudes are small can be attributed to the reactive current components resulted from the LC input filter as well as imperfect tuning of the primary LCCL network. Even though $v_{\rm grid}$ was assumed to be an ideal sinusoidal voltage source for reducing the complexity of the mathematical model, under experimental conditions $v_{\rm grid}$ was contaminated

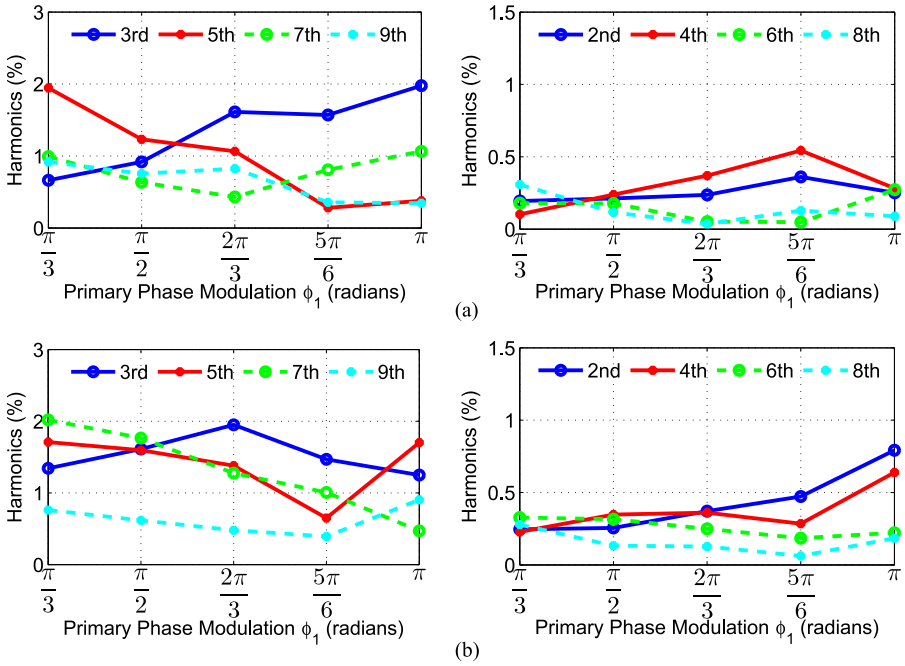

Fig. 15. Odd and even harmonics of grid currents for (a) forward power and (b) reverse power.

with a considerable low-order harmonic content. Thus, the LC low-pass filter draws reactive currents that correspond to each harmonic component of v_{grid}, even though they are not accounted for in the mathematical model. It is apparent from (16) that the reactive current component of i_{grid} is independent of θ. Thus, the harmonic results obtained for the forward power flow should be slightly different from those obtained for the reverse power flow. This causes slight differences in harmonic magnitudes for the forward power and reverse power operation of the system, as further seen by comparing Fig. 15(a) with Fig. 15(b).

According to the IEEE standard 1547, odd harmonics of the grid current up to the ninth harmonic must be less than 4%, whereas even harmonics up to the eighth harmonic must be retained below 1% for grid-tie inverters or converters. Therefore, it is obvious from Fig. 15(a) and (b) that the grid harmonic content of the prototype meets the criteria defined by the standards.

Fig. 16 illustrates the THD of the grid current i_{grid} [THD] up to the 50th harmonic of the prototype for forward and reverse power operation against the primary phase modulation φ_1, which again ranges from $\pi/3$ to π. As seen from Fig. 15(a) and (b), the overall grid current harmonic content for reverse power operation is marginally higher than that of the forward power operation. Hence, the i_{grid} [THD] for the forward power operation is slightly lower than that of the reverse power operation as depicted in Fig. 16. As noticeable from (16), the significance of the reactive current component of i_{grid} becomes more apparent at lower power levels. Thus, the i_{grid} [THD] peaks at 4.8% and 5.1% for forward and reverse power operation, respectively, at $\varphi_1 = \pi/3$ and then maintains a steady lower trend with increasing φ_1. The voltage THD of v_{grid} during the experiment was measured as 2.1%. This causes the LC filter to draw more reactive current components, hence, a higher i_{grid} [THD] in contrast to a situation with a lower voltage THD. Nevertheless, the

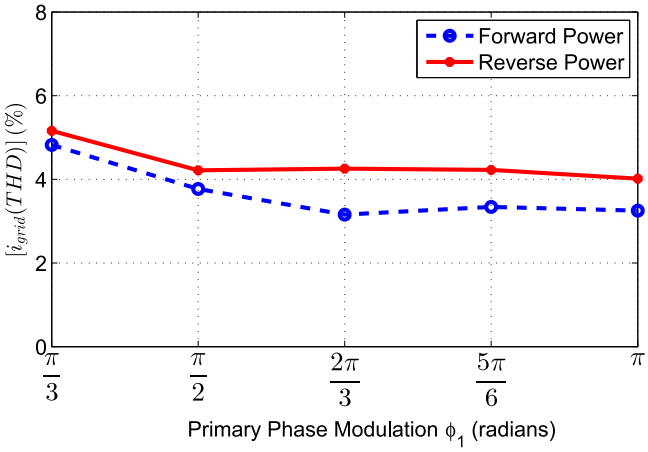

Fig. 16. THD of grid current.

forward i_{grid} [THD] values meet the 5% limit defined by the IEEE standard 1547 for the considered operational range, whereas the reverse i_{grid} [THD] values remain within the limit set by the standards for $\pi/2 \leq \varphi_1 \leq \pi$.

In order to investigate the quality of the grid current at a lightly loaded condition, the prototype was operated with a lower primary phase modulation of $\pi/12$ for both directions of power flow at $\theta = \pm\pi/2$. The harmonic magnitudes of i_{grid} up to the 50th order are illustrated in Fig. 17(a) and (b) for forward and reverse power operation, respectively. As evident from Fig. 17(a) and (b), harmonic content of the forward i_{grid} is slightly lower than that of the reverse i_{grid}. As a result, the forward i_{grid} [THD] of the prototype system was found to be 9.4%, whereas the reverse i_{grid} [THD] was measured as 10.6%. As calculated from (16) and (17), the magnitude of the reactive current component

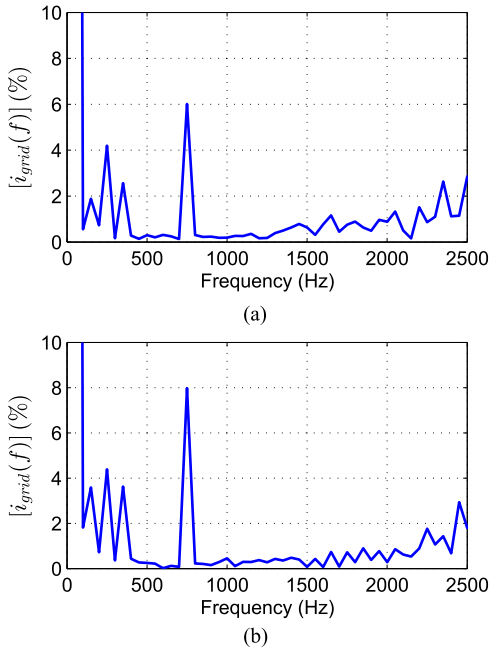

Fig. 17. Harmonic spectrum of $i_{\rm grid}$ when lightly loaded at $\varphi_1 = \pi/12$ for (a) forward power and (b) reverse power.

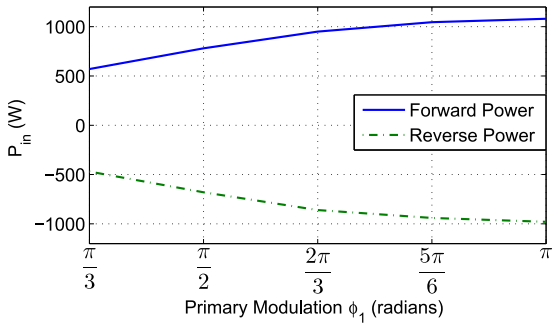

Fig. 18. Power throughput of the system.

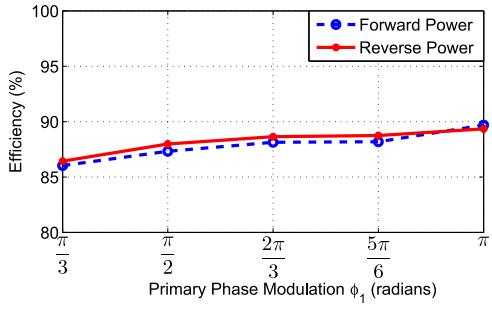

Fig. 19. Overall efficiency of the system.

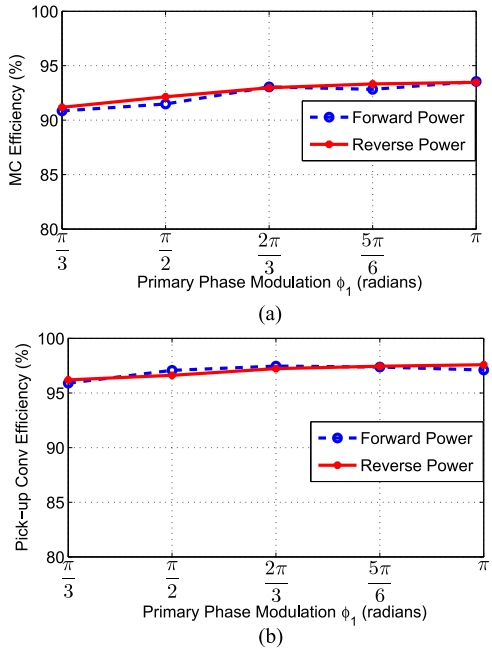

Fig. 20. Converter efficiencies. (a) MC and (b) IPT pick-up converter.

of $i_{\rm grid}$ is over 60% of that of $i_{\rm grid,dom}$. Thus, the shape of $i_{\rm grid}$ significantly deviates from a sinusoidal waveform and causes a higher $i_{\rm grid}$ [THD]. Nonetheless, even at a power throughput of 10% of the rated power, $i_{\rm grid}$ [THD] has exceeded the standard limits by less than 6% only.

D. Power and Efficiency

The variation of power $P_{\rm in}$ drawn by the experimental prototype as well as the power supplied to the grid, when the primary phase modulation φ_1 is increased from $\pi/3$ to π, is shown in Fig. 18. $P_{\rm in}$ is measured from the grid side for the both directions of power flow. The power drawn from the grid by the experimental prototype at $\theta = -\pi/2$ corresponds to forward power profile in Fig. 18 adhering to (22), whereas the reverse power flow at $\theta = \pi/2$ corresponds to the negative power profile. As predicted by (22), the magnitude of power increases with increasing φ_1 for both forward and reverse power flow. When the power flow is in the forward direction, the losses incurred by the prototype are supplied by the grid. On the other hand, the dc voltage source on the pick-up side supplies the losses incurred by the prototype for the reverse power flow. Therefore, the magnitude of the forward power profile is slightly higher than that of the reverse power profile, as evident from Fig. 18.

The overall efficiency of the experimental prototype, from the grid to the dc voltage source on the pick-up side, is shown in Fig. 19 for both directions of power flow at different primary modulation values. As evident from Fig. 19, the efficiency profile of the prototype for the forward power flow is similar to that of the reverse power flow in general. The experimental prototype exhibits its highest efficiency of 89.6% at $\varphi_1 = \pi$ for the forward power operation, whereas the highest efficiency for the reverse power operation is 89.3%. Furthermore, it is observed that the overall efficiency decreases with decreasing primary phase modulation levels. This can be explained using the individual efficiencies of MC and the IPT pick-up converter illustrated in Fig. 20(a) and (b), respectively. The current $i_{\rm pi}$ drawn by the MC is independent of φ_1 as evident from (15). As a result, $i_{\rm pi}$, which leads to conduction losses in the MC, remain

constant regardless of the variations in φ_1. Hence, the efficiency of the MC increases with increasing φ_1 or the power throughput of the system. On the contrary, $i_{\rm si}$, which leads to conduction losses in the IPT pick-up converter, is dependent upon the primary phase modulation φ_1. Therefore, a significant increase in the efficiency of the IPT pick-up converter is not apparent with increasing φ_1, as shown in Fig. 20(b).

E. Discussion

Although the accuracy of the proposed mathematically model is successfully verified experimentally under laboratory conditions, it is derived based on the assumption that both the primary and pick-up LCL networks are perfectly tuned. However, in practice, the values of the components can deviate from their rated values over time due to component aging and operating temperature variations. Substantial changes in component values essentially increase the degree of detuning of the resonant networks and lead to reactive power circulation. In case of a detuned primary, the MC must provide the reactive power requirement of the detuned primary resonant network. This leads to a reduction in the efficiency as well as the active power throughput of the MC. Moreover, in a practical system the air gap between the primary and pick-up pads is subjected to change. An increase in air gap causes a decrease in the coefficient of coupling k. Hence, the maximum power throughput of the system decreases in such cases. In order to maintain a fixed power throughput regardless of variations in k, a closed-loop controller can be employed as discussed in [26].

V. Conclusion

This paper has proposed a single-phase MC-based bidirectional contactless grid interface for V2G and G2V applications. The proposed system overcomes drawbacks such as inclusion of bulky and expensive dc-link capacitors, input inductors, and high grid current distortion of previously reported systems. The bidirectional switches of the proposed MC are operated at a frequency that is equal to the resonant frequency by means of a four-step current commutation algorithm based on the output current direction. A comprehensive mathematical model that estimates the steady-state converter voltages, currents, grid current, and the power drawn from the grid has been proposed. A modulation strategy for attenuation of grid current harmonics has been derived utilizing the mathematical model. As a result, bulky low-pass filters, which are typically found in MC-based systems, have been eliminated. The system' s ability to regulate the magnitude as well as the direction of the power flow has been demonstrated by presenting experimental results obtained from a 1-kW experimental prototype. Theoretical results have shown excellent agreement with experimental results, validating the accuracy of the mathematical model. Owing to the proposed modulation strategy, THD of the grid current has maintained within the acceptable limits over the majority of the considered operational range of the system even in the existence of a distorted grid voltage.

References

[1] A. Green and J. Boys, "10 kHz inductively coupled power transfer-concept and control," in *Proc. 5th Int. Conf. Power Electron. Variable-Speed Drives*, Oct. 1994, pp. 694–699.

[2] P. Sergeant and A. Van den Bossche, "Inductive coupler for contactless power transmission," *IET Elect. Power Appl.*, vol. 2, no. 1, pp. 1–7, Jan. 2008.

[3] D. Ahn and S. Hong, "Wireless power transmission with self-regulated output voltage for biomedical implant," *IEEE Trans. Ind. Electron.*, vol. 61, no. 5, pp. 2225–2235, May 2014.

[4] P. Si, A. Hu, S. Malpas, and D. Budgett, "A frequency control method for regulating wireless power to implantable devices," *IEEE Trans. Biomed. Circuits Syst.*, vol. 2, no. 1, pp. 22–29, Mar. 2008.

[5] A. RamRakhyani and G. Lazzi, "On the design of efficient multi-c telemetry system for biomedical implants," *IEEE Trans. Biomed. Circuits Syst.*, vol. 7, no. 1, pp. 11–23, Feb. 2013.

[6] S. Hui and W. Ho, "A new generation of universal contactless battery charging platform for portable consumer electronic equipment," *IEEE Trans. Power Electron.*, vol. 20, no. 3, pp. 620–627, May 2005.

[7] V. T. Nguyen, S. H. Kang, J. H. Choi, and C. W. Jung, "Magnetic resonance wireless power transfer using three-coil system with single planar receiver for laptop applications," *IEEE Trans. Consum. Electron.*, vol. 61, no. 2, pp. 160–166, May 2015.

[8] A. Sample, B. Waters, S. Wisdom, and J. Smith, "Enabling seamless wireless power delivery in dynamic environments," *Proc. IEEE*, vol. 101, no. 6, pp. 1343–1358, Jun. 2013.

[9] G. Covic and J. Boys, "Modern trends in inductive power transfer for transportation applications," *IEEE J. Emerg. Sel. Topics Power Electron.*, vol. 1, no. 1, pp. 28–41, Mar. 2013.

[10] V. Jiwariyavej, T. Imura, and Y. Hori, "Coupling coefficients estimation of wireless power transfer system via magnetic resonance coupling using information from either side of the system," *IEEE J. Emerg. Sel. Topics Power Electron.*, vol. 3, no. 1, pp. 191–200, Mar. 2015.

[11] J. Huh, S. Lee, C. Park, G.-H. Cho, and C.-T. Rim, "High performance inductive power transfer system with narrow rail width for on-line electric vehicles," in *Proc. IEEE Energy Convers. Congr. Expo.*, Sep. 2010, pp. 647–651.

[12] U. Madawala and D. Thrimawithana, "A bidirectional inductive power interface for electric vehicles in V2G systems," *IEEE Trans. Ind. Electron.*, vol. 58, no. 10, pp. 4789–4796, Oct. 2011.

[13] J. Miller, O. Onar, C. White, S. Campbell, C. Coomer, L. Seiber, R. Sepe, and A. Steyerl, "Demonstrating dynamic wireless charging of an electric vehicle: The benefit of electrochemical capacitor smoothing," *IEEE Power Electron. Mag.*, vol. 1, no. 1, pp. 12–24, Mar. 2014.

[14] H. Nguyen, C. Zhang, and M. Mahmud, "Optimal coordination of G2V and V2G to support power grids with high penetration of renewable energy," *IEEE Trans. Transport. Electrific.*, vol. 1, no. 2, pp. 188–195, Aug. 2015.

[15] M. Yilmaz and P. Krein, "Review of battery charger topologies, charging power levels, and infrastructure for plug-in electric and hybrid vehicles," *IEEE Trans. Power Electron.*, vol. 28, no. 5, pp. 2151–2169, May 2013.

[16] J. Sexauer, K. McBee, and K. Bloch, "Applications of probability model to analyze the effects of electric vehicle chargers on distribution transformers," *IEEE Trans. Power Syst.*, vol. 28, no. 2, pp. 847–854, 2013.

[17] R. Miskiewicz, A. Moradewicz, and M. Kazmierkowski, "Contactless battery charger with bi-directional energy transfer for plug-in vehicles with vehicle-to-grid capability," in *Proc. IEEE Int. Symp. Ind. Electron.*, 2011, pp. 1969–1973.

[18] M. Kazmierkowski and A. Moradewicz, "Unplugged but connected: Review of contactless energy transfer systems," *IEEE Ind. Electron. Mag.*, vol. 6, no. 4, pp. 47–55, Dec. 2012.

[19] S. Weerasinghe, D. Thrimawithana, and U. Madawala, "Modeling bidirectional contactless grid interfaces with a soft dc-link," *IEEE Trans. Power Electron.*, vol. 30, no. 7, pp. 3528–3541, Jul. 2015.

[20] *IEEE Standard for Interconnecting Distributed Resources With Electric Power Systems*, IEEE Standard 1547-2003, pp. 1–28, Jul. 2003.

[21] N. Burany, "Safe control of four-quadrant switches," in *Proc. IEEE Ind. Appl. Soc. Annu. Meeting Conf. Rec.*, Oct. 1989, vol. 1, pp. 1190–1194.

[22] N. X. Bac, D. Vilathgamuwa, and U. Madawala, "A SiC-based matrix converter topology for inductive power transfer system," *IEEE Trans. Power Electron.*, vol. 29, no. 8, pp. 4029–4038, Aug. 2014.

[23] A. Ecklebe, A. Lindemann, and S. Schulz, "Bidirectional switch commutation for a matrix converter supplying a series resonant load," *IEEE Trans. Power Electron.*, vol. 24, no. 5, pp. 1173–1181, May 2009.
[24] V. Oghafi and A. Radan, "Bidirectional switch commutation for high frequency UPF matrix converter supplying inductive power transfer system," in *Proc. Power Electron., Drive Syst. Technol. Conf.*, Feb. 2014, pp. 422–427.
[25] D. Thrimawithana and U. Madawala, "A generalized steady-state model for bidirectional IPT systems," *IEEE Trans. Power Electron.*, vol. 28, no. 10, pp. 4681–4689, Oct. 2013.
[26] A. Swain, S. Devarakonda, and U. Madawala, "Modeling, sensitivity analysis, and controller synthesis of multipickup bidirectional inductive power transfer systems," *IEEE Trans. Ind. Informat.*, vol. 10, no. 2, pp. 1372–1380, May 2014.

Saranga Weerasinghe (S'12) received the B.Sc. Eng. (Hons.) in electrical engineering from the University of Moratuwa, Moratuwa, Sri Lanka, in 2007. He is currently working toward the Ph.D. degree in electrical and electronic engineering at the University of Auckland, Auckland, New Zealand.

From 2007 to 2012, he worked as an Electrical Engineer for ABB AG, Mannheim, Germany. His research interests include power electronics, inductive power transfer, and matrix converters.

Udaya K. Madawala (M'95–SM'06) received the B.Sc. (Hons.) degree in electrical engineering from the University of Moratuwa, Moratuwa, Sri Lanka, in 1987, and the Ph.D. degree in power electronics from The University of Auckland, Auckland, New Zealand, in 1993.

After working in industry, he joined The University of Auckland in 1997, where he is currently a Full Professor in the Department of Electrical and Computer Engineering. His research interests include power electronics, inductive power transfer, and renewable energy, and he is a Consultant to industry.

Dr. Madawala is an IEEE volunteer and serves as an Associate Editor for the IEEE TRANSACTIONS ON INDUSTRIAL ELECTRONICS and the IEEE TRANSACTIONS ON POWER ELECTRONICS. He is a Member of the Power Electronics Technical Committee of the IEEE Industrial Electronics Society and the Sustainable Energy Systems Committee of the IEEE Power Electronics Society.

Duleepa J. Thrimawithana (M'09) received the B.E. degree in electrical engineering (with First Class Hons.) and the Ph.D. degree in power electronics both from The University of Auckland, Auckland, New Zealand, in 2005 and 2009, respectively.

From 2005 to 2008, he worked in collaboration with Tru-Test Ltd. in Auckland as a Research Engineer in the areas of power converters and high-voltage pulse generator design. He joined the Department of Electrical and Computer Engineering, The University of Auckland in 2009, where he is currently a Senior Lecturer. His main research interests include wireless power transfer, power electronics, and renewable energy.

Dr. Thrimawithana is the Chairman of the Joint Chapter of IEEE Industrial Electronics and Industrial Applications Society, New Zealand (North). He has coauthored more than 80 international journal and conference publications, and holds eight patent families on wireless power transfer technologies with several pending. In recognition of his outstanding contributions to engineering as an early career researcher, he received the Jim and Hazel D. Lord Fellowship in 2014.